

10 Simple Blade Design

Flow deflection in turbomachines is established by stator and rotor blades with prescribed geometry that includes inlet and exit *camber angles*, *stagger angle*, *camber line*, and *thickness distribution*. The blade geometry is adjusted to the stage velocity diagram which is designed for specific turbine or compressor flow applications. Simple blade design methods are available in the open literature (see References). More sophisticated and high efficiency blade designs developed by engine manufacturers are generally not available to the public. An earlier theoretical approach by Joukowski [1] uses the method of conformal transformation to obtain cambered profiles that can generate lift force. The mathematical limitations of the conformal transformation do not allow modifications of a cambered profile to produce the desired pressure distribution required by a turbine or a compressor blade design. In the following, a simple method is presented that is equally applicable for designing compressor and turbine blades. The method is based on (a) constructing the blade *camber line* and (b) superimposing a predefined *base profile* on the camber line. With regard to generating a base profile, the conformal transformation can be used to produce useful profiles for superposition purposes. A brief description of the Joukowski transformation explains the methodology of symmetric and a-symmetric (Cambered) profiles. The transformation uses the complex analysis which is a powerful tool to deal with the potential theory in general and the potential flow in particular. It is found in almost every fluid mechanics textbook that has a chapter dealing with potential flow. While they all share the same underlying mathematics, the style of describing the subject to engineering students differ. A very compact and precise description of this subject matter is found in an excellent textbook by Spurk [2].

10.1 Conformal Transformation, Basics

Before treating the Joukowski transformation, a brief description of the method is given below. We consider the mapping of a circular cylinder from the z -plane onto the ζ -plane, Fig. 10.1. Using a mapping function, the region outside the cylinder in the z -plane is mapped onto the region outside another cylinder in the ζ -plane. Let P and Q be the corresponding points in the z - and ζ -planes respectively.

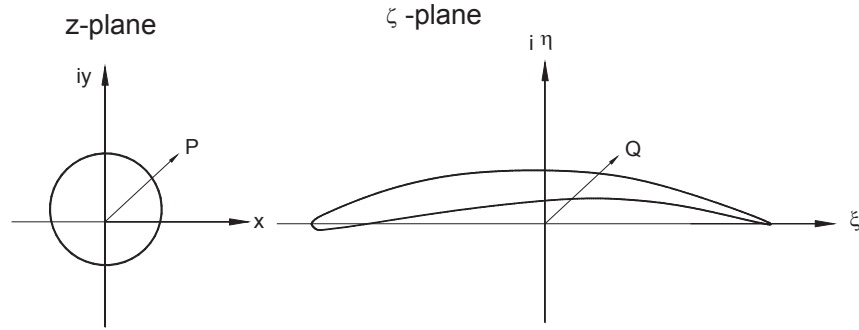


Fig. 10.1: Conformal transformation of a circular cylinder onto an airfoil

The potential at the point P is

$$F(z) = \Phi + i\Psi \quad (10.1)$$

The point Q has the same potential, and we obtain it by insertion of the mapping function

$$F(z) = F(z(\zeta)) = F(\zeta) \quad (10.2)$$

Taking the first derivative of Eq. (10.2) with respect to ζ , we obtain the complex conjugate velocity \bar{V}_ζ in the ζ plane from

$$\bar{V}_\zeta(\zeta) = \frac{dF}{d\zeta}. \quad (10.3)$$

Considering z to be a parameter, we calculate the value of the potential at the point z . Using the transformation function $\zeta = f(z)$, we determine the value of ζ which corresponds to z . At this point ζ , the potential then has the same value as at the point z . To determine the velocity in the ζ plane, we form

$$\frac{dF}{d\zeta} = \frac{dF}{dz} \frac{dz}{d\zeta} = \frac{dF}{dz} \left(\frac{d\zeta}{dz} \right)^{-1} \quad (10.4)$$

after introducing Eq. (10.3) into (10.4) and considering $\bar{V}_z(z) = dF/dz$, Eq. (10.4) is rearranged as

$$\bar{V}_\zeta(\zeta) = \bar{V}_z(z) \left(\frac{d\zeta}{dz} \right)^{-1} \quad (10.5)$$

Equation (10.5) expresses the relationship between the velocity in ζ -plane and the one in z -plane. Thus, to compute the velocity at a point in the ζ - plane, we divide the velocity at the corresponding point in the z -plane by $d\zeta/dz$. The derivative $dF/d\zeta$ exists at all points where $d\zeta/dz \neq 0$. At singular points with $d\zeta/dz = 0$, the complex conjugate velocity in the ζ plane $\bar{V}_\zeta(\zeta) = dF/d\zeta$ becomes infinite if it is not equal to zero at the corresponding point in the z -plane.

10.1.1 Joukowski Transformation

The conformal transformation method introduced by Joukowski allows mapping an unknown flow past a cylindrical airfoil to a known flow past a circular cylinder. Using the method of conformal transformation, we can obtain the direct solution of the flow past a cylinder of an arbitrary cross section. Although numerical methods of solution of the direct problem have now superseded the method of conformal mapping, it has still retained its fundamental importance. In what follows, we shall examine several flow cases using the *Joukowski* transformation function:

$$\zeta = f(z) = z + \frac{a^2}{z}, \text{ with } z = re^{i\theta}, \quad \zeta = \xi + i\eta \quad (10.6)$$

10.1.2 Circle-Flat Plate Transformation

Decomposing Eq. (10.6) into its real and imaginary parts, we obtain:

$$\xi = \left(r + \frac{a^2}{r} \right) \cos\theta, \quad \eta = \left(r - \frac{a^2}{r} \right) \sin\theta \quad (10.7)$$

The function $f(z)$ maps a circle with radius $r = a$ in the z -plane onto a “slit” in the ζ plane. Equation (10.7) delivers the coordinates:

$$\xi = 2a \cos \theta, \quad \eta = 0 \quad (10.8)$$

with ξ as a real independent variable in the ζ -plane. As the point P with the angle θ moves in z -plane from 0 to 2π , Fig. 10.2, its image p' moves from $+2a$ to $-2a$ in the ζ -plane with the complex potential $F(z)$.

The potential $F(z)$ is:

$$F(z) = V_\infty \left(z + \frac{R^2}{z} \right) \quad (10.9)$$

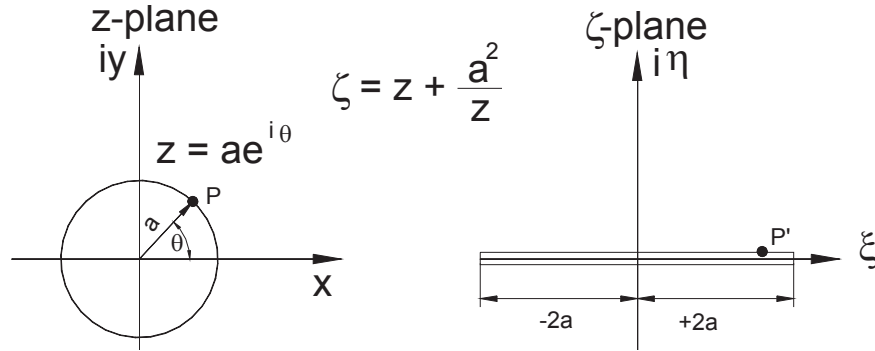


Fig. 10.2: Transformation of a circle onto a slit (straight line section)

Setting $R = a$, the Joukowski transformation function directly provides the potential in the ζ -plane as

$$F(\zeta) = V_\infty \zeta \quad (10.10)$$

10.1.3 Circle-Ellipse Transformation

For this transformation, the circle center is still at the origin of the z -plane. Now, if we map a circle with radius b which is smaller or larger than the mapping constant a , we obtain an ellipse. Replacing r by b ($b \neq a$), Eq. (10.7) becomes

$$\xi = \left(b + \frac{a^2}{b}\right)\cos\Theta, \quad \eta = \left(b - \frac{a^2}{b}\right)\sin\Theta \quad (10.11)$$

Eliminating θ from Eq. (10.11), we find:

$$\cos^2\theta = \left(\frac{\xi}{b + a^2/b}\right)^2, \quad \sin^2\eta = \left(\frac{\eta}{b - a^2/b}\right)^2 \quad (10.12)$$

and with $\sin^2\theta + \cos^2\theta = 1$, we obtain the equation of ellipse as:

$$\left(\frac{\xi}{b + a^2/b}\right)^2 + \left(\frac{\eta}{b - a^2/b}\right)^2 = 1 \quad (10.13)$$

Equation (10.13) describes an ellipse, plotted in Fig. 10.3, with the major and minor axes which are given as the denominators in Eq. (10.13). In Fig. 10.3, $b > a$, however any ellipse may be constructed by varying the ratio b/a .

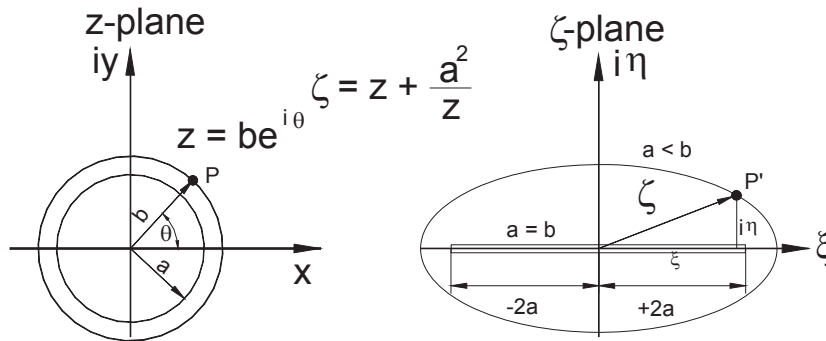


Fig. 10.3: Conformal transformation of a circle to an ellipse

10.1.4 Circle-Symmetric Airfoil Transformation

A set of symmetrical airfoils can be constructed by shifting the center of the circle with the radius b by Δx along the x -axis on the z -plane as shown in Fig. 10.4.

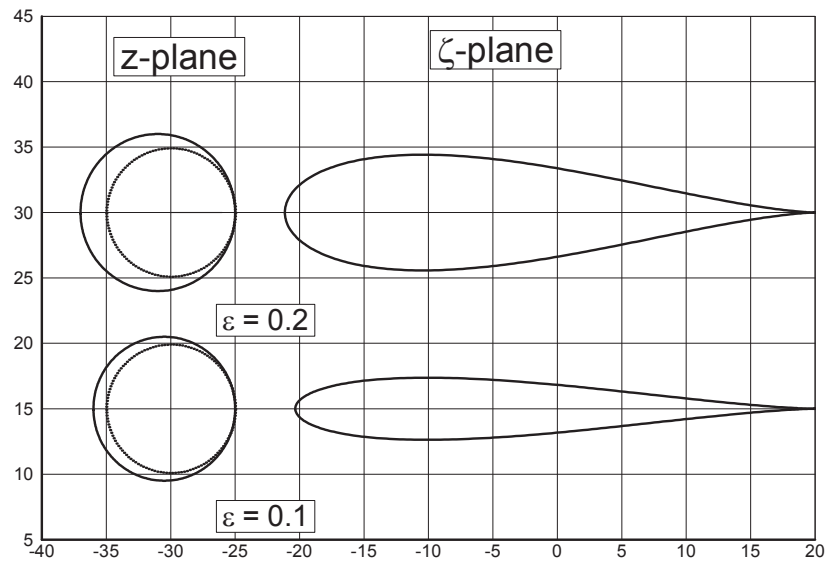


Fig. 10.4: Transformation of a circle into a symmetric airfoil

An eccentricity $\epsilon = e/a$ with $e = \Delta x$ is defined that determines the thickness of the airfoil. The radius of the circle is determined by:

$$b = (1 + \epsilon)a \quad (10.14)$$

Thus, the magnitude of the eccentricity defines the slenderness of the airfoil. For $\varepsilon = 0$, the circle is mapped into a slit, as seen in Fig. 10.3. Due to zero flow deflection, the symmetrical airfoils at zero-angle of attack do not generate circulation and, therefore, no lift. Similar profiles can be used as *base profiles* in compressor and turbine blade design to be superimposed on the *camberline*. Since these profiles have a sharp trailing edge (zero thickness), they cannot be used in practical applications because of stress concentration at the trailing edge. This can be avoided by placing a certain radius at the trailing edge as shown in Fig. 10.5.



Fig. 10.5: Symmetric profile constructed by conformal transformation, (a) with sharp trailing edge, (b) same profile with trailing edge radius

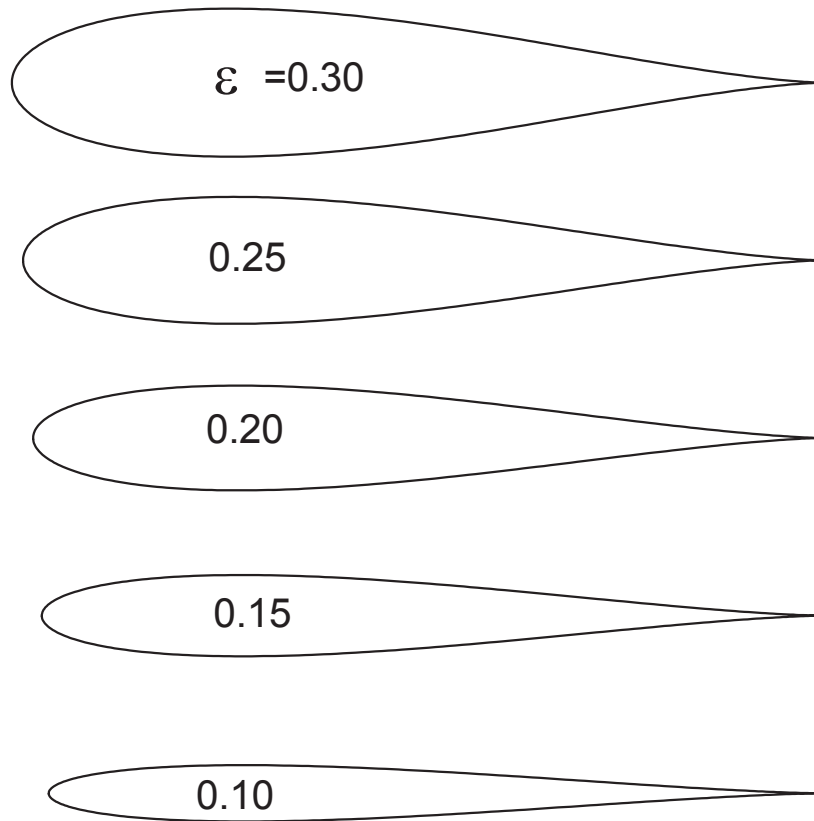


Fig. 10.6: Example of a systematic generation of base profiles varying the eccentricity ε

Figure 10.6 exhibits a systematic generation of base profiles by varying the eccentricity ϵ . Turbine blades that are exposed to a frequent off-design operation condition have generally a larger leading edge radius than those that operate almost in design point. In this case, $\epsilon > 0.15$ may be chosen. A FORTRAN program is presented in the Appendix that calculates the symmetric profiles shown in Fig. 10.6

10.1.5 Circle-Cambered Airfoil Transformation

To generate airfoils that produce circulation and, therefore, lift, the profile must be cambered. In this case, the circle with the radius b is displaced horizontally as well as vertically relative to the origin of the circle with the radius a . To generate a systematic set of profiles, we need to know how the circle b is to be displaced relative to the origin of the circle a . Only three parameters define the shape of the cambered profiles. These are: (a) Eccentricity e , angle α , and the intersection angle β . With these three parameters, the displacements in x- and y -directions as well as the radius of the circle b to be mapped onto the ζ -plane are calculated using the following relations from Fig.10.7.

$$a = \overline{OB}, \quad b = \overline{AB} = a \cos \gamma + a \epsilon \cos(\beta/2)$$

$$\gamma = \arcsin\left(\frac{e}{a} \sin \beta/2\right) = \arcsin(\epsilon \sin \beta/2)$$

$$b/a = \cos \gamma + \epsilon \cos(\beta/2)$$

$$\overline{OC} = a \sin \gamma = e \sin(\beta/2)$$

$$\epsilon = e/a$$

$$\Delta x = \overline{OD} = e \cos(\alpha + \beta/2)$$

$$\Delta y = \overline{DA} = e \sin(\alpha + \beta/2)$$

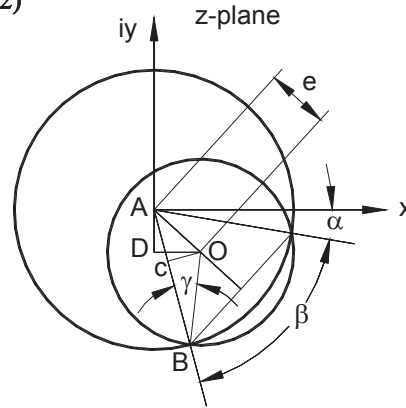


Fig. 10.7: Construction of cambered airfoils

Figure 10.7 shows a family of profiles generated by varying the above parameters. Starting with a small eccentricity of $\epsilon = 10\%$, we set $\beta = 0^\circ$ and vary the angle α from -10° to -30° . The resulting configuration indicates that the two circles have tangents at the angle α . At this small eccentricity, slender profiles are generated that resemble low subsonic compressor blade profiles. Increasing the magnitude of α results in an increase of the profile cambers. If the angle β is different from zero, then the two circles intersect each other, as shown in Fig.10.7. This is also shown in Fig. 10.8 with $\epsilon = 0.2$, $\beta = 60^\circ$ and α varied from -10° to -30° .

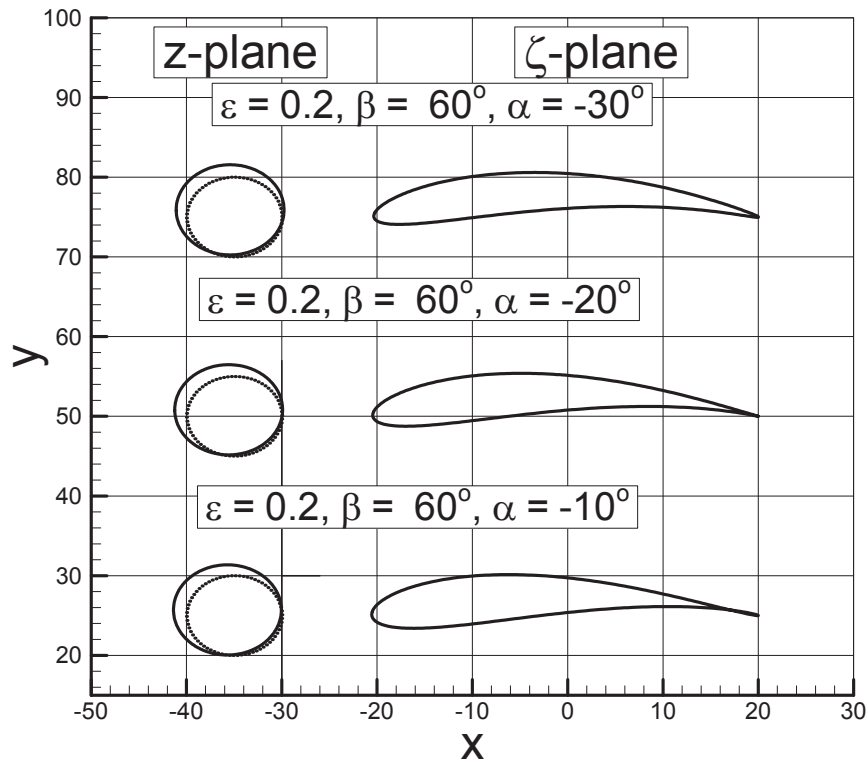


Fig. 10.8: Cambered profiles constructed by conformal transformation

For $\varepsilon > 0.2$, the resulting profiles resemble turbine profiles, however, they cannot be used in practice because the resulting cascade channel does not yield a continuous acceleration.

10.2 Compressor Blade Design

The major parameter for determining the shape of a compressor blade is the Mach number. For low-subsonic to intermediate-subsonic Mach range ($M_1 = 0.1$ to 0.6), NACA-65 profiles [3] give a relatively high pressure at a reasonably high efficiency. For intermediate Mach numbers, *double circular arc* (DCA) and *multi-circular arc* (MCA) profiles may be used. Surface pressure measurements by Cumpsty [4] show that at an inlet Mach number of $M_1 = 0.6$ at the design incidence, the NACA-65 and DCA profiles have comparable pressure distributions. However, due to a sharp leading edge, the DCA-profiles may have higher profile losses than the NACA-65 series when operating at off-design conditions. For high subsonic Mach range ($M_1 > 0.6$), DCA or MCA profiles are used. Controlled diffusion profiles CD are used for transonic Mach ranges in order to reduce the shock losses.

Supersonic compressors require s-shaped blades with sharp leading edges to avoid the shock detachment.

10.2.1 Low Subsonic Compressor Blade Design

In Chapter 6.2, it was shown that for an inviscid flow, the lift force can be expressed as:

$$\mathbf{F} = \rho V_{\infty} \times \Gamma, \quad \text{where} \quad \Gamma = \oint \mathbf{V} d\mathbf{c} \quad (10.15)$$

This relation shows that the lift force can exist if there is circulation around the airfoil. As we saw, the circulation was directly related to the flow deflection from the cascade inlet to the exit, which is shown in Fig. 10.9.

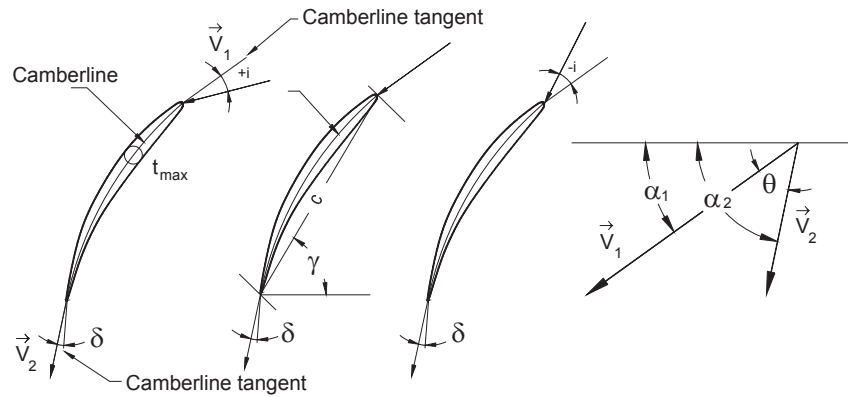


Fig. 10.9: Compressor cascade nomenclature, c = chord length, t_{\max} = maximum thickness, γ = cascade stagger angle, Θ = cascade flow deflection angle, i = flow incidence angle, δ = flow deviation angle. For $i > 0$ the actual deflection $\Theta > \Theta_{\text{design}}$

For an incidence free ($i = 0$) flow, the velocity vector at the inlet is tangent to the camber line. Likewise, for a deviation free ($\delta = 0$) exit flow, the velocity vector is tangent to the camber line at the cascade exit, as seen in Fig. 10.9. Once the compressor stage velocity diagram is constructed, the deflection angle θ and, thus, the circulation Γ is known. The problem now is to find the corresponding blade profile for a given circulation. For a compressor blade which generally has a small flow deflection, the circulation Γ can be thought of as the sum of infinitesimal vortices with the intensity $d\Gamma$. If we distribute the vortices along the blade chord and consider the specific circulation at an arbitrary point x to be:

$$\gamma(x) = \frac{d\Gamma}{dx} \quad (10.16)$$

the integrating Eq. (10.16) yields:

$$\Gamma = \int_0^c \gamma(x) dx \quad (10.17)$$

The vortex $d\Gamma$, located at the point ζ , induces a velocity at an arbitrary point x , that can be calculated from Bio-Sawart's law. Figure 10.10 shows the distribution of discrete vortices along the chord (left) and their induced velocity (right).

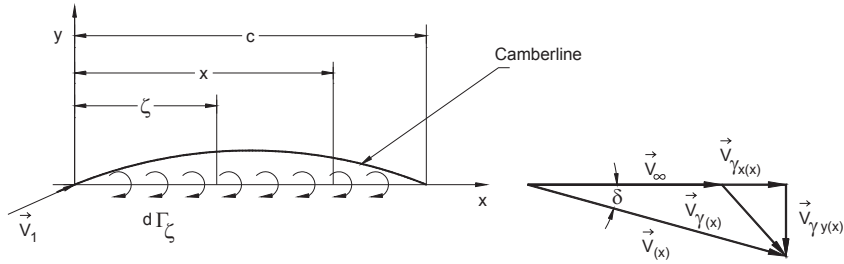


Fig. 10.10: Vortex distribution along the blade chord and induced velocity

An induced velocity in y -direction is:

$$dV_{\gamma y}(x) = -\frac{d\Gamma_{\zeta}}{2\pi(x - \zeta)} \quad (10.18)$$

and in the x -direction:

$$V_{\gamma x}(x) = \pm \frac{\gamma(x)}{2}, \quad (- \text{ sign for } x > \zeta) \quad (10.19)$$

The integration of Eq. (10.19) gives the total velocity induced at x by the vortices distributed at ζ :

$$V_{\gamma y}(x) = -\frac{1}{2\pi} \int_0^c \frac{\gamma(\zeta) d\zeta}{(x - \zeta)} \quad (10.20)$$

The induced velocity for the incidence angle $i = 0$ is shown in Fig. 10.10. Superimposing the induced velocity $V_{\gamma}(x)$ on V_{∞} , we get the contour velocity $V(x)$ around the profile. Since the direction of this velocity must be identical with the slope of the camber line,

$$\tan \delta = \frac{dy(x)}{dx} = \frac{V_y(x)}{V_1 + V_x(x)} \quad (10.21)$$

and since the induced velocity component $V_{yx}(x) \ll V_1$, it follows that

$$\frac{dy(x)}{dx} = \frac{V_y(x)}{V_1} \quad (10.22)$$

Introducing Eq. (10.18) into (10.22):

$$\frac{dy(x)}{dx} = -\frac{1}{2\pi V_1} \int_0^c \frac{\gamma(\zeta) d\zeta}{x - \zeta} \text{ for } i = 0 \quad (10.23)$$

and for considering a small incidence angle i , we find:

$$i + \frac{dy(x)}{dx} = -\frac{1}{2\pi V_1} \int_0^c \frac{\gamma(\zeta) d\zeta}{x - \zeta} \quad (10.24)$$

Now, we introduce the lift coefficient for the camber line and label it with the superscript *:

$$C_L^* = \frac{F^*}{\frac{\rho}{2} V_1^2 c} = \frac{\rho \Gamma V_1}{\frac{\rho}{2} V_1^2} = \frac{2\Gamma}{V_1 c} \quad (10.25)$$

We assume that the lift force induced by a discrete vortex is linearly proportional to the blade lift. This uniform lift distribution assumption results in:

$$\frac{d\Gamma_\zeta}{d\zeta} = \frac{\Gamma}{c} \quad (10.26)$$

and so:

$$\frac{d\Gamma_\zeta}{d\zeta} = \gamma(\zeta) = \frac{C_L^*}{2} V_1 \quad (10.27)$$

Inserting Eq. (10.27) into (10.24) and setting for $i = 0$:

$$\frac{dy(x)}{dx} = \frac{C_L^*}{4\pi} \int_0^c \frac{d\zeta}{x - \zeta} \quad (10.28)$$

The first integration of Eq. (10.28) yields:

$$\frac{dy(x)}{dx} = \frac{C_L^*}{4\pi} \ln \left(\frac{1 - \frac{x}{c}}{\frac{x}{c}} \right) \quad (10.29)$$

The second integration determines the coordinate for the camber line:

$$\frac{y(x)}{c} = -\frac{C_L^*}{4\pi} \left[\left(1 - \frac{x}{c} \right) \ln \left(1 - \frac{x}{c} \right) + \frac{x}{c} \ln \left(\frac{x}{c} \right) \right] \quad (10.30)$$

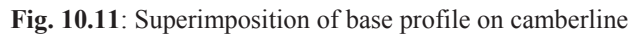
This is the equation of the camber line for the NACA-compressor blades. The maximum camber is at $x/c = 0.5$

$$\frac{y_{\max}}{c} = \frac{C_L^*}{4\pi} \ln 2 \quad (10.31)$$

Superimposing the Base Profile: With Eq. (10.30), we are able to design the compressor blade camberline at a particular position where the lift coefficient is already calculated. To construct the profile, we need a base profile to superimpose on the camber. The base profile is given for NACA-65 series. For a profile with chord c the camber line coordinates are:

$$\begin{aligned} x_c &= \frac{x}{c} c \\ y_c &= \frac{y}{c} c \end{aligned} \quad (10.32)$$

where the subscript c represents the camber line. The next step is to superimpose the base profile either from Section 10.1.4 or from Table 10.1 on the camber.


$$\frac{t}{c} = \left(\frac{t}{c}\right)_{ref} \frac{\left(\frac{t}{c}\right)_{\max}}{\left(\frac{t}{c}\right)_{\max ref}} \quad (10.33)$$
$$\left. \begin{aligned} x &= x_c - \left(\frac{t}{2}\right) \sin \vartheta \\ y &= y_c + \left(\frac{t}{2}\right) \cos \vartheta \end{aligned} \right\} \quad (10.34)$$

and for the pressure side, where $\overline{cp} = t/2$:

$$\left. \begin{aligned} x &= x_c + \left(\frac{t}{2} \right) \sin \vartheta \\ y &= y_c - \left(\frac{t}{2} \right) \cos \vartheta \end{aligned} \right\} \quad (10.35)$$

The angle ϑ is calculated from Eq. (10.29):

$$\frac{dy(x)}{dx} = \tan \vartheta = \frac{C_L^*}{4\pi} \ln \left(\frac{1 - \frac{x_c}{c}}{\frac{x_c}{c}} \right) \quad (10.36)$$

In addition to the base profiles listed in Section 10.1.4, a NACA-base profile for subsonic compressors and a base profile for subsonic turbines used in industrial practice as well as in research are listed in Table 1 and 2 with the nomenclature shown in Fig. 10.12. The maximum thickness for compressors is around $t_{\max}/c = 10\%$, whereas for turbines it may vary from 15% to 18%.

Table 10.1: Thickness distribution of a NACA-65 compressor base profile

| | | | | | | | | | |
|----------|-------|-------|-------|-------|-------|-------|-------|-------|-------|
| ξ | 0.00 | 0.50 | 0.75 | 1.25 | 2.5 | 5.0 | 7.5 | 10 | 15 |
| $f(\xi)$ | 0.00 | 0.772 | 0.932 | 1.690 | 1.574 | 2.177 | 2.641 | 3.040 | 3.666 |
| ξ | 20 | 25 | 30 | 35 | 40 | 45 | 50 | 55 | 60 |
| $f(\xi)$ | 4.143 | 4.503 | 4.760 | 4.924 | 4.996 | 4.963 | 4.812 | 4.530 | 4.146 |
| ξ | 65 | 70 | 75 | 80 | 85 | 90 | 95 | 100 | |
| $f(\xi)$ | 3.682 | 3.156 | 2.584 | 1.987 | 1.385 | 0.810 | 0.306 | 0 | |

Table 10.2: Thickness distribution of a turbine base profile

| | | | | | | | | | |
|----------|-------|-------|------------------------------------|-------|---------------------|-------|-------|-------|-------|
| ξ | 0.00 | 5.0 | 10.00 | 15.00 | 20.00 | 25.00 | 30.00 | 35.00 | 40.00 |
| $f(\xi)$ | 0.00 | 8.40 | 11.11 | 13.00 | 14.40 | 14.90 | 15.00 | 14.40 | 13.50 |
| ξ | 45.00 | 50.00 | 55.00 | 60.00 | 65.00 | 70.00 | 75.00 | 85.00 | 90.00 |
| $f(\xi)$ | 12.40 | 11.20 | 10.10 | 8.90 | 7.70 | 6.70 | 5.70 | 3.80 | 3.00 |
| ξ | 95.00 | 100.0 | $r_l/c = 0.030$ $r_T/c = 0.009$ | | $t_{\max}/c = 0.15$ | | | | |
| $f(\xi)$ | 2.10 | 0.00 | | | | | | | |

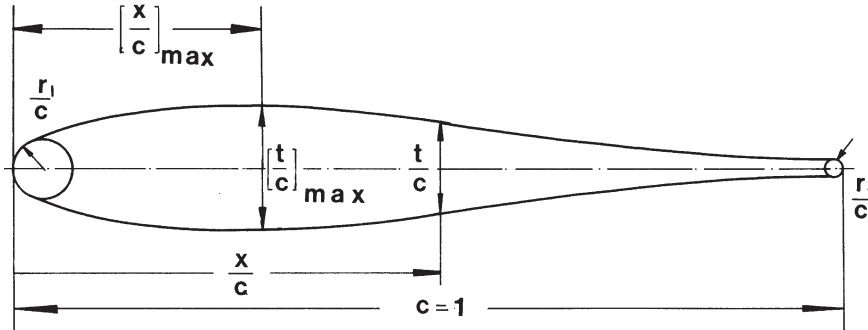


Fig. 10.12: Schematic of a base profile to be superimposed on camberline, $\xi = x/c$, $t/c = f(\xi)$

It should be noted that the base profiles with lower eccentricity shown in Fig. 10.6 may also be used for subsonic compressor design.

Summary, simple compressor blade design steps:

1. Calculate C_L^* from velocity diagram using Eq. (10.25)
2. To find (y/c) , calculate $y(x)/c$ from Eq. (10.30)
3. Calculate ϑ from Eqs. (10.25) and (10.36).
4. If $(t/c)_{\max}$ is different from $(t/c)_{\max \text{ ref.}}$, then introduce new $(t/c)_{\max}$ into Eq. (10.33) and use the data for the reference base profile.
5. With the actual t , calculate the suction surface coordinates from Eq. (10.34) and the pressure surface coordinates from Eq. (10.35)
6. Smooth the profile and make sure, there is no discontinuity and no waviness on the surface. This is done by taking the first derivative of the surface function. Any CAD system has the capability to do this task.

The above procedure is equally valid for the turbine profile design also.

10.2.2 Compressors Blades for High Subsonic Mach Number

Double circular arc (DCA) and multi-circular arc (MCA) profiles are used particularly for compressors operating at intermediate and high subsonic inlet Mach numbers ($M > 0.6$). Considering a particular cross section through a compressor cascade as shown in Fig. 10.13, the suction and pressure surfaces of a DCA-profile consist of two circular arcs. The suction and pressure surfaces of MCA-profiles however, may consist of several circular arcs. The arc must have the same slopes at the joints to avoid surface discontinuities. This can be assured by plotting the first surface derivative.

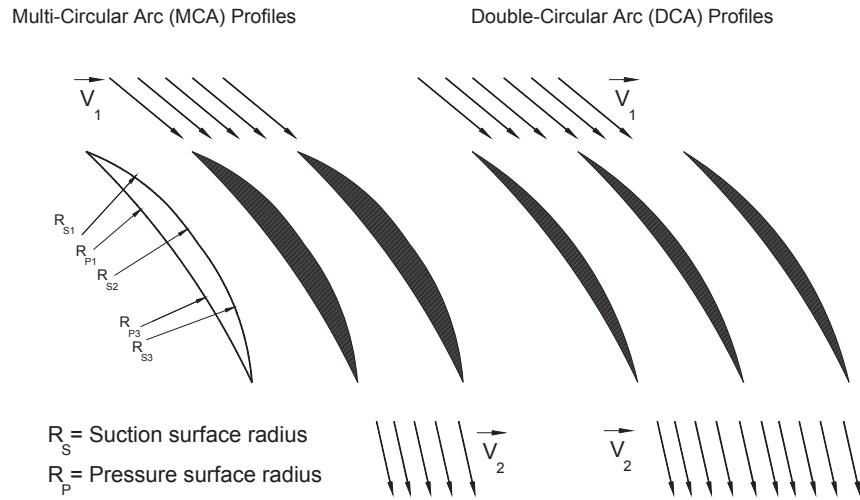


Fig. 10.13: DCA and MCA profiles for high subsonic Mach number applications

The following criteria dictate the selection of a particular profile for high subsonic compression application:

1. The inlet Mach number
2. Incidence tolerance with regard to the profile losses
3. Pressure distribution determining the lift coefficient
4. Drag forces determining the blade profile loss

(1) and (4) can be combined to arrive at the optimum lift/drag ratio, which we have treated in Chapter 6.

10.2.3 Transonic, Supersonic Compressor Blades

For compressors operating at transonic and supersonic Mach numbers, blade design efforts are concentrated at keeping the shock losses at a minimum level. In doing so, it is important to accurately determine the shock angle. This topic is extensively discussed in Chapter 16. Figure 10.14 shows a supersonic compressor cascade with an inlet Mach number $M_\infty > 1$. The incoming supersonic flow impinges on the sharp leading edge and forms a weak oblique shock, followed by an expansion fan. Passing through the shock front, the Mach number, although smaller, remains supersonic. Expansion waves are formed along the suction surface (convex side) of the blade from the leading edge L to the point e where the subsequent Mach wave at point e intersects the adjacent blade leading edge.

Regarding the transonic compressors, the research efforts resulted in the design of *controlled diffusion blades* that almost eliminate shock losses [5], [6] and [7].

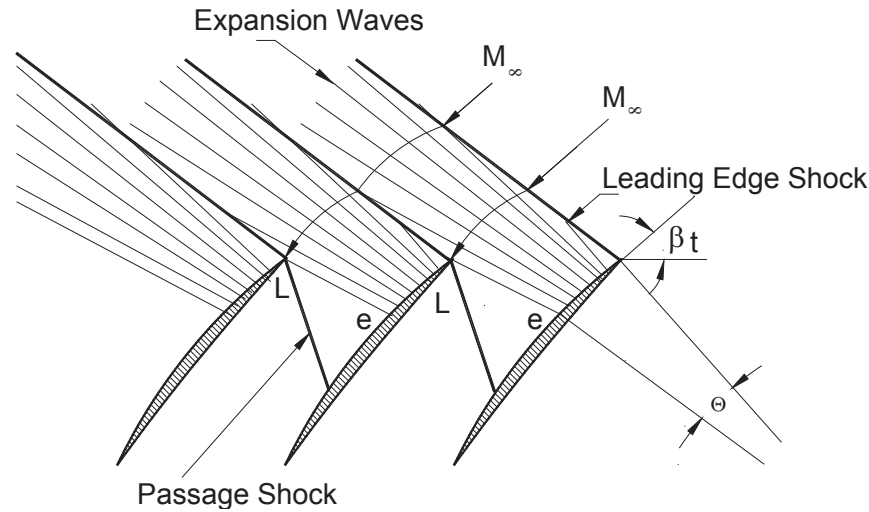


Fig. 10.14: Schematic of a supersonic compressor cascade the supersonic inlet mach number, expansion wave and passage shocks

For compressors operating in the supersonic Mach range, the so called S-profiles with sharp leading edges are used. The pressure and suction surfaces consist of multi-circular arcs with very small curvatures (large radii). Particular attention must be paid to the shock losses, as discussed in Chapters 7 and [8]. The flow decelerates within the convergent part by a system of oblique shock waves followed by a normal shock. Further deceleration is achieved by diffusion within the divergent part. As seen, these profiles have a slightly convergent inlet tangent to a throat which is followed by a slightly divergent channel.

10.3 Turbine Blade Design

Different turbine blade designs are discussed in literature among others, [9], [10], [11], [12], and [13]. Given the stage velocity diagram with the flow velocity vectors and angles, the corresponding blade profiles are constructed such that the flow angles at the inlet and exit are realized. This includes the incorporation of the design incidence and deviation into the design process as discussed in Chapter 9. Figure 10.15 schematically shows the velocity diagram and the corresponding velocity stator and rotor blades. Analogous to Section 10.2, the task here is designing the camberline on which a base profile will be superimposed. The camberline can be constructed from the inlet and exit flow angles under consideration of the incidence and deviation discussed in Chapter 9. This can be done graphically or numerically. Both methods are discussed in the following Section.

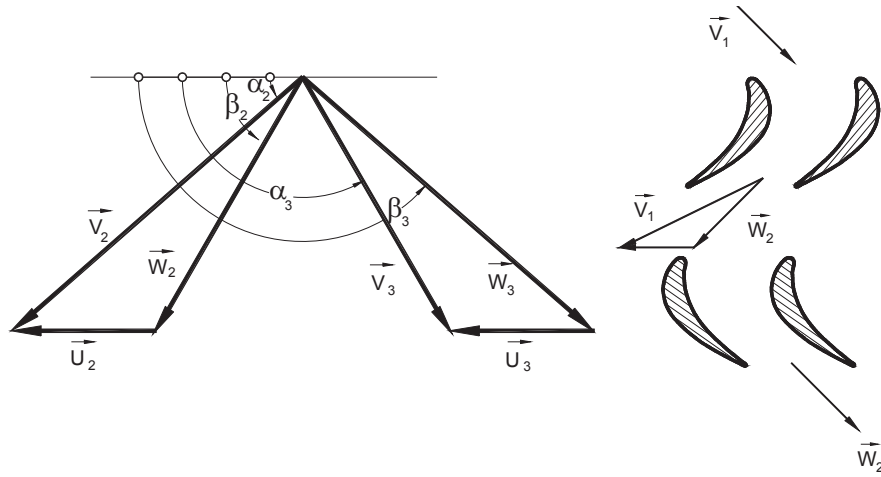


Fig. 10.15: Allocation of a set of stator and rotor blades to a given velocity diagram

10.3.1 Graphic Design of Camberline

Given a chord length $c = l$ and stagger angle γ , the tangents to the leading- and trailing-edge of the camberline to be determined are constructed by the inlet and exit metal angles as shown in Fig. 10.16. The latter is found from the stage velocity diagram under consideration of incidence and deviation angles that lead to α_{1c} and α_{2c} , Fig. 10.17.

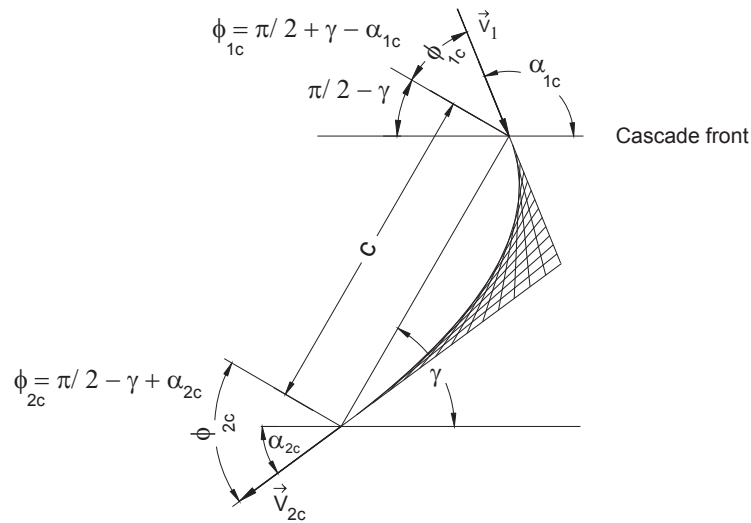


Fig. 10.16: Camber angle definitions: α_{1c} , α_{2c} = camber angles at the cascade inlet and exit, ϕ_{1c} , ϕ_{2c} = auxiliary angles.

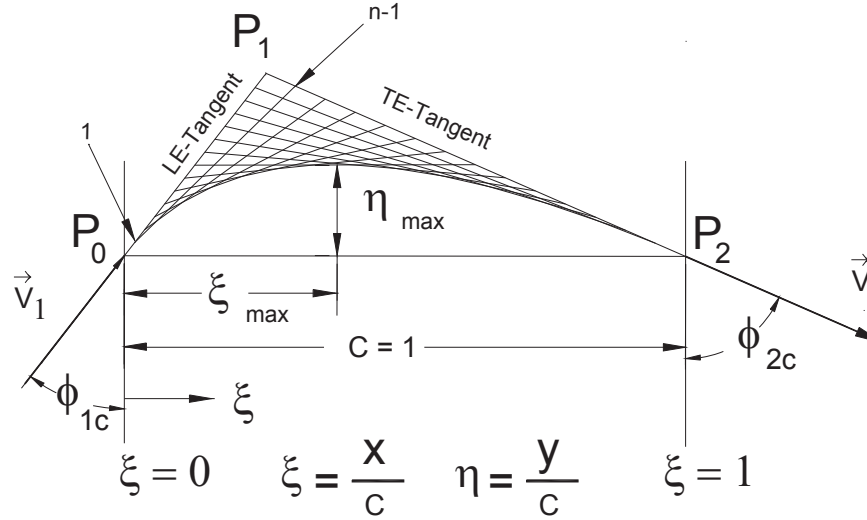


Fig. 10.17: Nomenclature of the quantities for constructing the camberline

The tangents intersect each other at the point P_1 and are subdivided into $n-1$ equal distances as shown in Fig. 10.17. Starting with the first point 1 at the leading edge (LE) tangent, a line is drawn to intersect the trailing edge (TE) tangent at point $n-1$. The following lines start at the second point on the LE-tangent and intersect the TE-tangent at $n-2$ and so on. The same procedure is repeated with first point at the TE-tangent starting with P_2 . The envelope of the inner region of the connecting lines is the camberline, as shown in Fig. 10.17.

10.3.2 Camberline Coordinates Using Bézier Curve

A similar camberline is constructed using Bézier polynomial presented, among others, in [14]. The general Bézier polynomial of degree n is given as:

$$\mathbf{B}(t) = \sum_{i=0}^n \binom{n}{i} (1-t)^{n-i} t^i \mathbf{P}_i \quad (10.37)$$

with \mathbf{P}_i as the given points, $t \in [0, 1]$ the curve parameter, and $\mathbf{B}(t)$ the position vector of the Bézier curve at the curve parameter t . For the purpose of designing the camberline, a quadratic Bézier curve is quite appropriate for a conventional turbine blade design. It reads:

$$\mathbf{B}(t) = (1-t)^2 \mathbf{P}_0 + 2(1-t)t \mathbf{P}_1 + t^2 \mathbf{P}_2 \quad (10.38)$$

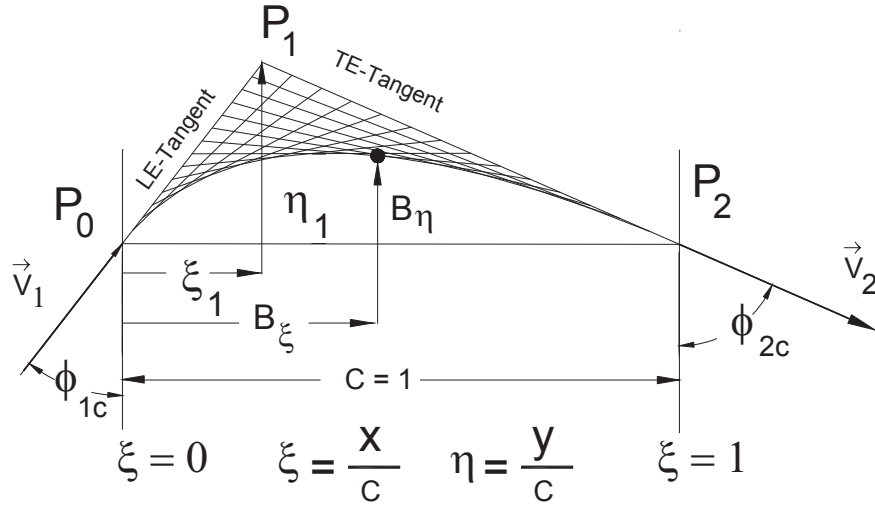


Fig. 10.18: Dimensionless quantities for calculating the Bézier curve

Before re-writing the Bézier formulation in terms of our nomenclature, we resort to Fig. 10.18, where the camber and Bézier quantities are shown.

Equation (10.38) reads

$$\begin{aligned}
 B_{\xi}(\xi) &= (1 - \xi)^2 P_{0_{\xi}} + 2(1 - \xi)\xi P_{1_{\xi}} + \xi^2 P_{2_{\xi}} \\
 B_{\eta}(\xi) &= (1 - \xi)^2 P_{0_{\eta}} + 2(1 - \xi)\xi P_{1_{\eta}} + \xi^2 P_{2_{\eta}}
 \end{aligned}
 \tag{10.39}$$

Considering the nomenclature in Fig. 10.18, the boundary conditions are:

$$\text{For } P_0: \quad \xi = 0: \quad P_{0_{\xi}} = 0, \quad P_{0_{\eta}} = 0$$

$$\text{For } P_1: \quad P_{1_{\xi}} = \frac{1}{1 + \frac{\cot \phi_{1c}}{\cot \phi_{2c}}}, \quad P_{1_{\eta}} = \frac{\cot \phi_{1c}}{1 + \frac{\cot \phi_{1c}}{\cot \phi_{2c}}}
 \tag{10.40}$$

$$\text{For } P_2: \quad \xi = 1: \quad P_{2_{\xi}} = 1, \quad P_{2_{\eta}} = 0$$

With Eq. (10.39), the coordinates of the camberline are calculated by varying the dimensionless variable ξ from 0 to 1. A smooth camberline is obtained by introducing a small increment $\xi = 0.01$ or less.

10.3.3 Alternative Calculation Method

Although a Bèzier curve provides a reasonable solution for camberline design, the position of the maximum thickness (ξ_{\max} , η_{\max}) may or may not be accurate. In this case, the following simpler method offers an appropriate alternative. The camber line can be described by a polynomial:

$$\eta = \sum_{v=0}^n a_v \xi^v \quad (10.41)$$

The coefficients a_v are obtained from the following boundary conditions:

$$\text{At } \xi = \frac{x}{c} = 0 \Rightarrow \eta = 0, \text{ and } \frac{d\eta}{d\xi} = \tan(\pi/2 - \phi_{1c}) \quad \text{BC1}$$

$$\text{At } \xi = \frac{x}{c} = 1 \Rightarrow \eta = 0, \text{ and } \frac{d\eta}{d\xi} = \tan(\pi/2 - \phi_{2c}) \quad \text{BC2}$$

$$\text{At } \xi = \xi_{\max} \Rightarrow \frac{\partial \eta}{\partial \xi} = 0 \quad \text{BC3}$$

where ξ_{\max} and η_{\max} are given. With the boundary conditions BC1 to BC3, five coefficients can be determined. The corresponding polynomial is of fourth order:

$$\eta = \sum_{v=0}^4 a_v \xi^v \quad (10.42)$$

or

$$\eta = a_0 + a_1 \xi + a_2 \xi^2 + a_3 \xi^3 + a_4 \xi^4 \quad (10.43)$$

From BC1, it follows immediately that $a_0 = 0$. It is important to ensure that there is no discontinuity on the profile surfaces. For this purpose, the final profile should be smoothed mathematically. For a highly deflected turbine cascade, the application of the above procedure may result in an inflection point. To prevent this, the camberline may be subdivided into two or more lower degree polynomials that tangent each other at the same slope. It should be pointed out that, for subsonic turbine blades with $r > 0.0\%$, the area between two adjacent blades must continuously converge, enabling the flow to accelerate continuously. For zero-degree reaction, the blade channel area must be constant throughout. Once the camberline is constructed, a turbine base profile is superimposed and the profile is generated, Fig.10.19.

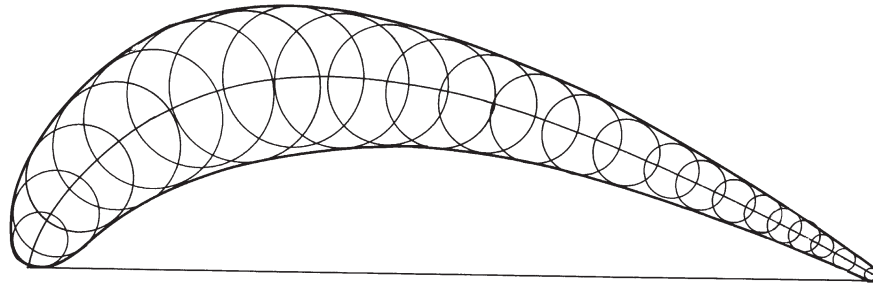


Fig. 10.19: Superposition of a base profile on the camber line

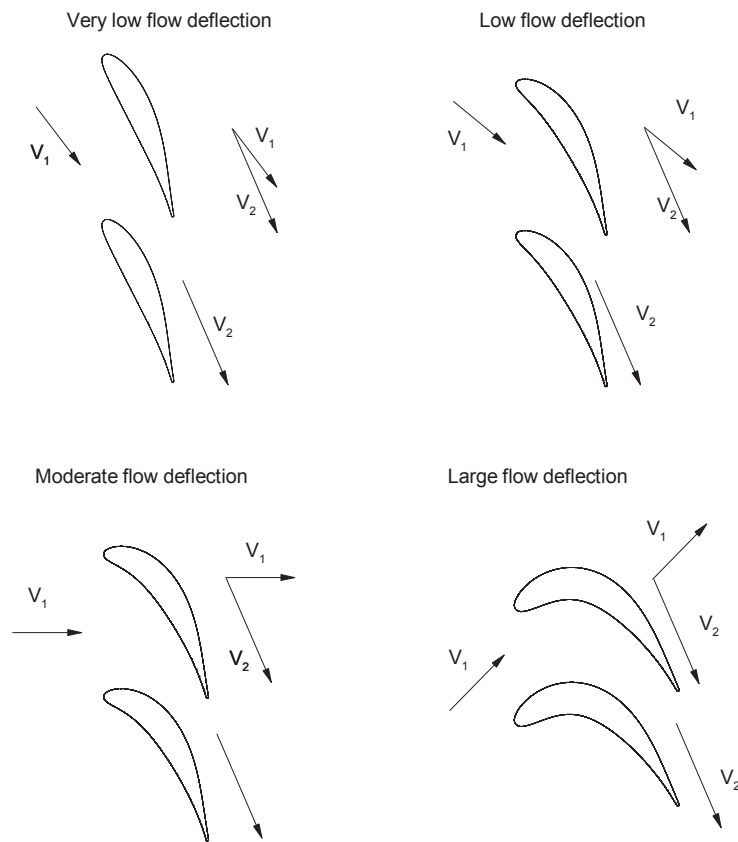


Fig. 10.20: An example of a systematic turbine blade design for different flow deflections

Applying the methods discussed above, four different conventional blade profiles are presented in Fig. 10.20 for different flow deflections. Moderate flow deflection blades are used in steam turbine design to keep the profile losses as small as possible. In contrast, the gas turbine engines, particularly the aircraft engines, use high deflection blades to keep the weight/thrust ratio as low as possible.

10.4 Assessment of Blades Aerodynamic Quality

The objective of a turbine stator or rotor blade design is to accomplish a certain flow deflection that is required to produce a prescribed amount of power per stage. Given the inlet and the exit flow angles resulting in a given flow deflection, an infinite number of blades with different shapes can be constructed that realize the above flow deflection. These blades, however, will have different boundary layer distributions on suction and pressure surfaces and, thus, different profile loss coefficients. Among the numerous possible designs, only one has the lowest loss coefficient, i.e., the optimum efficiency at the design operating point only. Figure 10.21 shows the pressure distribution along the suction and pressure surfaces of a high efficiency turbine blade at the design point. This blade type is sensitive to incidence changes caused by off-design operation.

If the operation conditions vary that result in a change of incidence angle, the losses may increase substantially. Thus, the operation condition of a turbine plays a crucial role in designing the blade. If the mass flow or the pressure ratio of a turbine component undergo frequent changes, the blades must be designed in such a way that their profile losses do not experience significant increases. Parameters determining

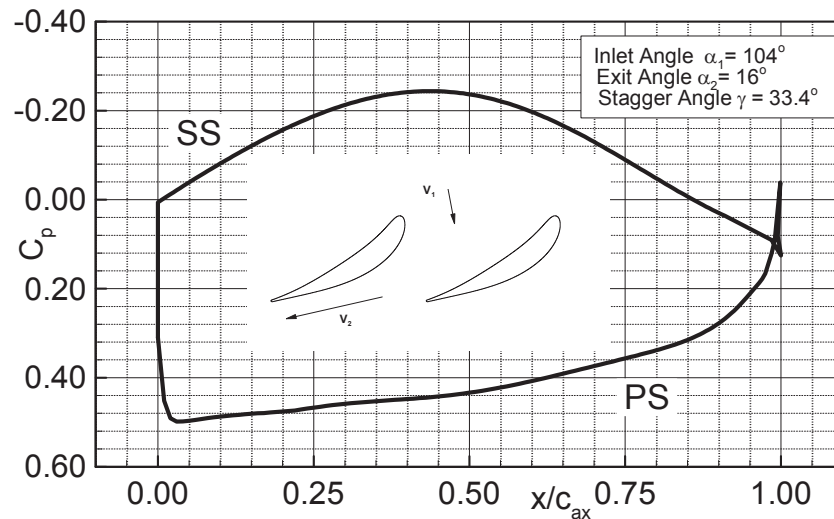


Fig. 10.21: Pressure distribution along the suction and pressure surfaces of a high efficiency turbine blade, *TPFL-Class Project 2010*

the efficiency and performance behavior of a turbine as a result of the boundary layer development on the suction and pressure surface are, among others, Reynolds number, Mach number, pressure gradient, turbulence intensity and unsteady inlet flow conditions. Of the above parameters, the geometry defines the pressure gradient which is, in the first place, responsible for the boundary layer development, separation and re-attachment. Since the pressure distribution is determined by the geometry and vice versa, the question arises as to how the blade geometry should be configured in order to establish a desired pressure distribution. This question has been the subject of numerous papers dealing with the *inverse blade design*, particularly for subcritical and supercritical compressor cascades [15], [16], and [17]. In context of this Chapter, we treat the question of the pressure distribution versus geometry from a simple physical point of view to establish a few criterions as a guideline for turbine blade design. The following example should demonstrate what criteria should be used in order to design a turbine blade that operates at a wide range of incidence changes without a substantial decrease of its efficiency:

1. With exception of the leading edge portion, the pressure gradient on the pressure and suction surfaces should not experience sign changes over a range of 60% to 70% of the blade axial chord.
2. Over the above range, the pressure gradient should be close to zero. This means that flow on both surfaces neither accelerates nor decelerates.
3. Over the rest of 30% to 40% of the blade surface, the flow should strongly accelerate.

Applying the criteria (1) through (3) associated with a moderately thick leading edge radius provides a turbine blade that is insensitive to adverse off-design operation conditions at a relatively high efficiency, Fig. 10.22.

Figure 10.23 shows the numerical calculation of the pressure coefficient versus the dimensionless axial chord. As seen, with exception of the leading edge portion the pressure distributions do not change over a wide range of incidence from -15° to $+21^\circ$. This numerical result is verified experimentally and presented in Figs. 10.24.

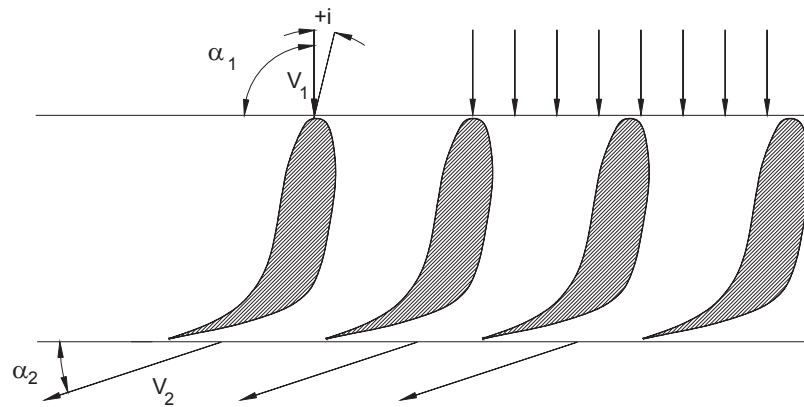


Fig. 10.22: A turbine cascade that fulfils the criteria (1) through (3)

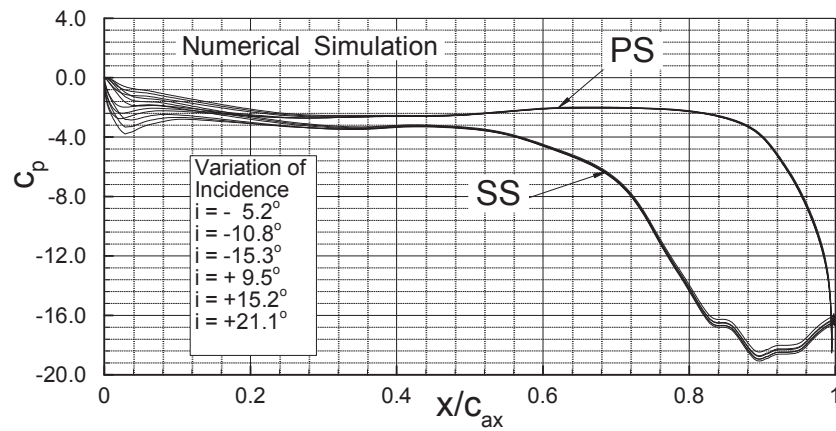


Fig. 10.23: Pressure distribution as a function of dimensionless axial chord with the incidence angle as parameter

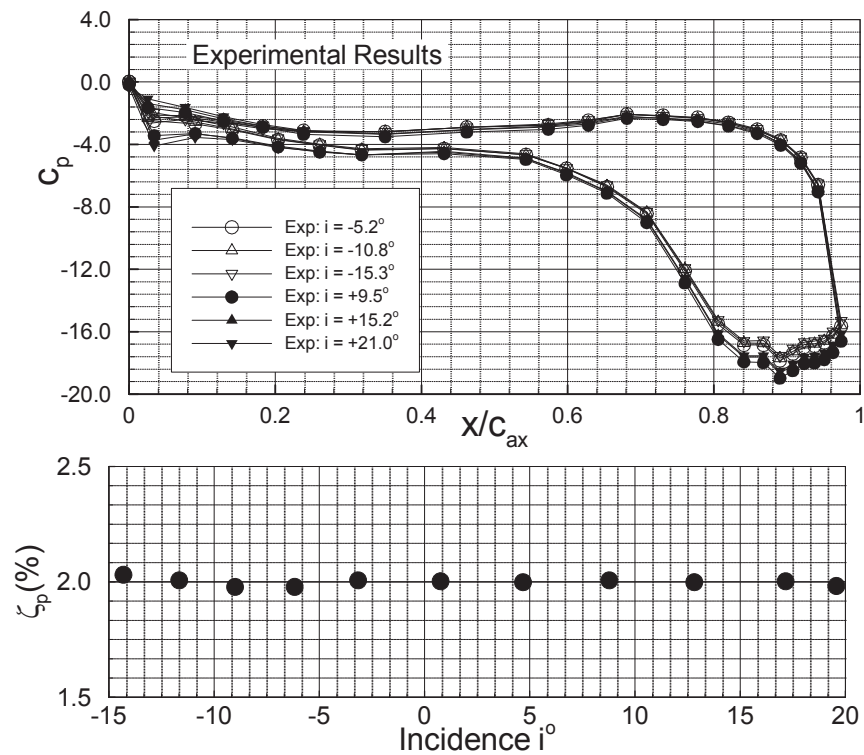


Fig. 10.24: Experimental pressure distribution as a function of dimensionless surface, total pressure loss coefficient as a function of incidence angle

Figure 10.24 shows the experimental verification of the numerical results presented in Fig. 10.23. It also shows the profile loss coefficient ζ_p as a function of the incidence angle. Here as in Fig. 10.23, the pressure distributions do not change over a wide range of incidences from -15° to $+21^\circ$. The results are in reasonable agreement with the numerical results, resulting in an approximate constant loss coefficient of 2%.

References

1. Joukowski, N.E.: Vortex Theory of Screw Propeller. I-IV, I-III, The forth paper published in the Transactions of the Office for Aerodynamic Calculations and Essays of the Superior Technical School of Moscow (in Russian). Also published in Gauthier-Villars et Cie (eds). *Théorie Tourbillonnaire de l'Hélice Propulsive*, Quatrième Mémoire. 123–146: Paris, in French (1918)
2. Spurk, J.H.: Fluid Mechanics. Springer, New York (1997)
3. NASA SP-36 NASA Report (1965)
4. Cumpsty, N.A.: Compressor Aerodynamics. Longman Group, New York (1989)
5. Hobson, D.E.: Shock Free Transonic Flow in Turbomachinery cascade. Ph.D-Thesis, Cambridge University Report CUED/A Turbo/65 (1979)
6. Schmidt, J.F.: Redesign and Cascade tests of a Supercritical Controlled Diffusion stator Blade Section. AIAA Paper 84-1207
7. Lakschminarayana, B.: Fluid Dynamics and Heat Transfer of Turbomachinery. John Wiley and Sons, Chichester (1995)
8. Schobeiri, M.T.: A New Shock Loss Model for Transonic and Supersonic Axial Compressors With Curved Blades. AIAA, Journal of Propulsion and Power 14(4), 470–478 (1998)
9. Teufelberger, A.: Choice of an optimum blade profile for steam turbines. Rev. Brown Boveri 2, 126–128 (1976)
10. Kobayashi, K., Honjo, M., Tashiro, H., Nagayama, T.: Verification of flow pattern for three-dimensional-designed blades. ImechE paper C423/015 (1991)
11. Jansen, M., Ulm, W.: Modern blade design for improving steam turbine efficiency. VDI Ber. 1185 (1995)
12. Emunds, R., Jennions, I.K., Bohn, D., Gier, J.: The computation of adjacent blade-row effects in a 1.5 stage axial flow turbine. ASME paper 97-GT-81, Orlando, Florida (June 1997)
13. Dunavant, J.C., Erwin, J.R.: Investigation of a Related Series of Turbine-blade Profiles in Cascade. NACA TN-3802 (1956)
14. Gerald, F.: Curves and Surfaces for Computer-aided Geometric Design, 4th edn. Elsevier Science & Technology Books, Amsterdam (1997)
15. Bauer, F., Garabedian, P., Korn, D.: Supercritical Wing Sections III. Springer, New York (1977)
16. Dang, T., Damle, S., Qiu, X.: Euler-Based Inverse Method for Turbomachine Blades: Part II—Three Dimensions. AIAA Journal 38(11) (2000)
17. Medd, A.J.: Enhanced Inverse Design Code and Development of Design Strategies for Transonic Compressor Blading. Ph.D. dissertation, Department of Mechanical Engineering, Syracuse University (2002)